



Interfacial chemical bond regulating the electronic coupling of $\text{ZnIn}_2\text{S}_4-x\text{-WO}_{3-x}$ for enhancing the photocatalytic pollutions degradation coupled with hydrogen evolution

Xiaomei Sun^{a,1}, Meiyang Song^{a,1}, Fei Liu^{a,*}, Haiyan Peng^a, Tianxiang Zhao^{a,*},
Shuang-Feng Yin^{b,*}, Peng Chen^{a,*}

^a Provincial Guizhou Key Laboratory of Green Chemical and Clean Energy Technology, Engineering Research Center of Efficient Utilization for Industrial Waste, School of Chemistry and Chemical Engineering, Guizhou University, Guiyang 550025, Guizhou, China

^b State Key Laboratory of Chemo/Biosensing and Chemometrics, Provincial Hunan Key Laboratory for Cost-effective Utilization of Fossil Fuel Aimed at Reducing Carbon-dioxide Emissions, College of Chemistry and Chemical Engineering, Hunan University, Changsha 410082, Hunan, China

ARTICLE INFO

Keywords:

Interfacial chemical bond
Z-scheme heterostructure
Electronic structure
 $\text{ZnIn}_2\text{S}_4-x\text{-WO}_{3-x}$
Photocatalytic pollutions degradation coupled with hydrogen evolution

ABSTRACT

Constructing Z-scheme heterostructure photocatalysts with a staggered band structure holds great potential to realize synergistic oxidation and reduction reactions. However, the Z-scheme heterostructure with interfacial vacancies significantly disturbs the behaviors of charge transfer and remains a challenging as well as urgent issue to exploit. Here, the ultrathin $\text{ZnIn}_2\text{S}_4-x\text{-WO}_{3-x}$ Z-scheme heterostructure (ZW) was synthesized via a facile in situ hydrothermal strategy. Experimental results and DFT calculations unveiled that the dual vacancies induced the formation of interfacial bonds. Importantly, the interfacial bonds tremendously modulate the electronic structure of heterostructure for enlarging the built-in electric field and reducing the aggregation effect of charge in the interface vacancies, which contributed to promoting charge transfer through the interface as well as exciton dissociation. Ultimately, the optimized ZW-4 exhibited an exceptional photocatalytic hydrogen evolution performance of $737.75 \mu\text{mol g}^{-1} \text{h}^{-1}$ and a pollution degradation rate greater than 99.99% without using any cocatalyst under visible light irradiation. Our work offers a deep insight into the ideal charge migration paths in highly efficient Z-scheme heterojunctions with vacancies.

1. Introduction

With the rapid development of science and technology, energy crises and environmental pollution are regarded as two major threats to current society [1–5]. In particular, organic pollutants with high toxicity and difficulty to degradation provide a challenging subject for researchers. Fortunately, the photocatalytic degradation of organic pollutants coupled with hydrogen generation (PPH) holds promise as a win-win strategy to produce clean energy and solve pollution problems [6–8]. However, most work still depends on the use of single model organics, expensive cocatalysts (such as Pt), or the replenishment of sacrificial additives, which seriously impedes the balanced development of PPH. Therefore, it is crucial and essential to develop highly efficient systems and provide clear synergistic mechanisms for the PPH [9].

Recently, the ternary metal sulfide ZnIn_2S_4 has attracted tremendous

attention in the field of photocatalytic degradation and hydrogen generation, owing to its appropriate band gap and favorable chemical stability [10,11]. However, individual semiconductors still face challenges such as fast recombination of charges and sluggish oxidation kinetics. Notably, constructing direct Z-scheme heterojunctions comprising an oxidation photocatalyst has been known to improve charge transport and photocatalytic activity [12,13]. Tungsten oxide (WO_3), a canonical n-type semiconductor, exhibited considerable advantages including visible light absorption [14,15], nontoxicity and strong oxidation ability, making it a promising candidate for constructing direct Z-scheme photocatalysts to take full advantage of redox properties. For example, Tang *et al.* prepared a Z-scheme $\text{WO}_3/\text{ZnIn}_2\text{S}_4$ photocatalyst that exhibited superior performance compared to that of a pure catalyst for the degradation of nitenpyram [16]. Li *et al.* designed a new Z-scheme Janus bilayer heterostructure to promote atomic-level charge transfer

* Corresponding authors.

E-mail addresses: ce.feiliu@gzu.edu.cn (F. Liu), txzhao3@gzu.edu.cn (T. Zhao), sf_yin@hnu.edu.cn (S.-F. Yin), pchen3@gzu.edu.cn (P. Chen).

¹ These authors contribute equally to this work.

and separation by coupling $\text{Vs-ZnIn}_2\text{S}_4$ and WO_3 nanosheets [17]. In fact, such heterojunction systems simultaneously promote light absorption and charge transfer while maintaining their own redox capacity [18]. Yet, poor interfacial contact in Z-scheme heterojunctions severely affects photocatalytic efficiency [19]. Moreover, the lower internal electric driving force cannot ensure the neutralization of holes and electrons at the interface, resulting in poor performance. Importantly, the spatial separation of Z-scheme heterojunctions and the synergistic effect of interface structure are still a challenging and urgent issue to exploit [20].

In this study, an ultrathin $\text{ZnIn}_2\text{S}_{4-x}\text{-WO}_{3-x}$ Z-scheme heterostructure was designed and synthesized via a facile in situ hydrothermal strategy. Experimental results and DFT calculations unveiled that the dual vacancies induced the formation of interfacial bonds. Importantly, the interfacial bonds tremendously regulated the electronic structure for enhancing the compatibility of the heterojunction, which contributed to the enlarged built-in electric field for charge transfer and exciton dissociation at the interface. The photocatalyst exhibited an excellent photocatalytic hydrogen evolution performance ($737.75 \mu\text{mol g}^{-1} \text{h}^{-1}$) and a pollution degradation rate greater than 99.99%. This work offers a deep insight into the charge migration paths in highly efficient Z-scheme heterojunctions with vacancies.

2. Experimental section

2.1. Preparation of WO_3 (WO)

Generally, 1 g of $\text{Na}_2\text{WO}_4 \cdot 2 \text{H}_2\text{O}$ was dissolved in 50 mL of water. Then, 0.8 mL of lactic acid and 6.0 M HCl solution were added until the $\text{pH} = 1.00$. After stirring for 30 min, the mixture experienced a hydrothermal reaction at 120°C for 6 h using a Teflon-lined stainless-steel autoclave. After cooling to room temperature, hydrous WO_3 nanosheets were obtained by centrifugation, washing with deionized water and anhydrous ethanol for many times to remove impurities, placing in a vacuum drying oven and drying at 70°C for 12 h. Finally, hydrous WO_3 NPs were calcined in Ar gas at a heating rate of 2°C min^{-1} and maintained at 400°C for 2 h to obtain WO_3 .

2.2. Preparation of ZnIn_2S_4 with sulfur vacancies (ZIS)

0.4 mmol of $\text{Zn}(\text{CH}_3\text{COO})_2 \cdot 2 \text{H}_2\text{O}$, 0.8 mmol of $\text{InCl}_3 \cdot 4 \text{H}_2\text{O}$ and 1.6 mmol of thioacetamide (TAA) were dissolved in 30 mL deionized water and 30 mL anhydrous ethanol, stirring for 30 min. The mixture experienced a hydrothermal reaction at 180°C for 24 h. Finally, the product obtained by centrifugation, washing with deionized water and anhydrous ethanol for many times to remove impurities, placing in a vacuum drying oven and drying at 70°C for 12 h and designated as ZIS.

2.3. Preparation of $\text{ZnIn}_2\text{S}_{4-x}\text{-WO}_{3-x}$ (ZW)

To synthesize ZW composites, different amounts of WO_3 , 1.6 mmol of TAA, 0.4 mmol of $\text{Zn}(\text{CH}_3\text{COO})_2 \cdot 2 \text{H}_2\text{O}$ and 0.8 mmol $\text{InCl}_3 \cdot 4 \text{H}_2\text{O}$ were dispersed in a mixed solvent containing 30 mL water and 30 mL ethanol. After stirring for 30 min, the mixture experienced a hydrothermal reaction at 180°C for 24 h. Finally, the product obtained by centrifugation, washing with deionized water and anhydrous ethanol for many times to remove impurities, placing in a vacuum drying oven and drying at 70°C for 12 h. In this system, the selected molar ration of ZnIn_2S_4 and WO_3 are 10: 2, 10: 3, 10: 4, 10: 5, 10: 6 and are labeled as ZW-X (X = 2, 3, 4, 5 and 6).

2.4. Preparation of the random recombination of $\text{ZnIn}_2\text{S}_{4-x}/\text{WO}_{3-x}$ (RZW)

The prepared $\text{ZnIn}_2\text{S}_{4-x}$ and WO_{3-x} dispersed in 200 mL deionized water in equal mass ratios and ultrasonicated for 3 h. The mixture was

then centrifuged and dried at 70°C overnight to obtain the random recombination of $\text{ZnIn}_2\text{S}_{4-x}/\text{WO}_{3-x}$, which was named RZW.

2.5. Photodegradation of organic contaminant coupled with H_2 generation

Photodegradation of organic contaminant (Rhodamine (RhB), Crystal Violet (CV), Tetracycline (TC) and Methyl Orange (MO)) and simultaneous H_2 production has been implemented by the real-time monitoring reaction system with refrigeration cycle equipment (Fig. S1, supporting information, SI). In general, 20 mg of as prepared samples was dispersed in 50 mL of organic contaminant solution (40 mg L^{-1}). After stirring in the dark for 30 min, a 300 W xenon lamp ($\lambda > 420 \text{ nm}$) was irradiated. The H_2 production rate can be detected by the real-time monitoring of gas chromatography system (GC9790). The degradation rate of the organic contaminant was quantified using an ultraviolet spectrometer and ^1H NMR. The apparent quantum yield (AQY) can be calculated by our reported works [21,22].

3. Results and discussion

3.1. Morphology and structure

The $\text{ZnIn}_2\text{S}_{4-x}\text{-WO}_{3-x}$ Z-scheme heterojunction with the sulfur and oxygen vacancies was synthesized via a facile in situ hydrothermal strategy (Fig. 1a). The morphology of the samples was observed using scanning electron microscopy (SEM) and high resolution transmission electron microscopy (HRTEM). As shown in Fig. 1b and Fig. S2 (SI), the ZW-4 sample has a hierarchical flower-like structure self-assembled numerous of nanosheets, which is in accordance with transmission electron microscope (TEM) results (Fig. 1c). From Fig. 1d-e, the ZW-4 exhibited two lattice spacings of 0.31 and 0.32 nm, which are related to the (101) facet of WO_3 and the (311) facet of ZnIn_2S_4 , respectively [18,19], suggesting the heterojunction was successfully synthesized. Importantly, close interfacial contact between WO_3 and ZnIn_2S_4 can be observed, which can conduce to the charge transfer across the phase interface [23]. From atomic force microscope (AFM) image (Fig. S3, SI), the ZIS, WO_3 , RZW and ZW-4 were measured as 11, 27, 12 and 9 nm, suggesting the typical two dimensions (2D) structure of as prepared samples, which contributes to ultrafast carrier dynamics transfer and active site exposure [24]. Moreover, the element mapping image illustrated the uniform dispersion of W, O, Zn, In and S elements in the ZW-4 heterojunction (Fig. 1f-j), indicating a tight and uniform heterojunction was successfully constructed through the designed hydrothermal route [25]. Meanwhile, the specific surface area of the ZIS, WO_3 , RZW and ZW-4 are equal to 45.3, 10.7, 29.4 and $49.4 \text{ m}^2 \text{g}^{-1}$ (Fig. S4, SI), proving that the ZW-4 could provide a large number of active sites for photocatalysis [26].

As exhibited in Fig. S5 (SI), the typical diffraction peaks of bare WO_3 at 23.71° , 28.77° , 34.07° and 55.63° were indexed as the (110), (101), (200) and (310) planes of WO_3 [27,28]. In addition, the peaks of bare ZnIn_2S_4 at 23.68° , 27.76° , 48.31° and 56.72° were in agreement with those of the hexagonal phase ZnIn_2S_4 [29]. Importantly, all the heterojunctions are harmony with the ZnIn_2S_4 and WO_3 [30].

3.2. Chemical bonding interface affect electronic structure

As shown in the Raman spectroscopy (Fig. 2a), three Raman bands around 131 , 305 and 345 cm^{-1} in ZIS are the longitudinal optical mode (LO_1), transverse optical mode (TO_2), and longitudinal optical mode (LO_2) of ZnIn_2S_4 [31], respectively. The band at 705 and 805 cm^{-1} are corresponded to the symmetric and asymmetric O-W-O bonds in WO_3 [32]. Two slight peaks situated at about 352 and 417 cm^{-1} can be assigned to the W-S bonding state, suggesting that the ZIS and WO_3 were intimately combined by W-S bond [33]. The intensity of Raman peaks in ZW-4 become weaker and broader and slight shift compared to that of

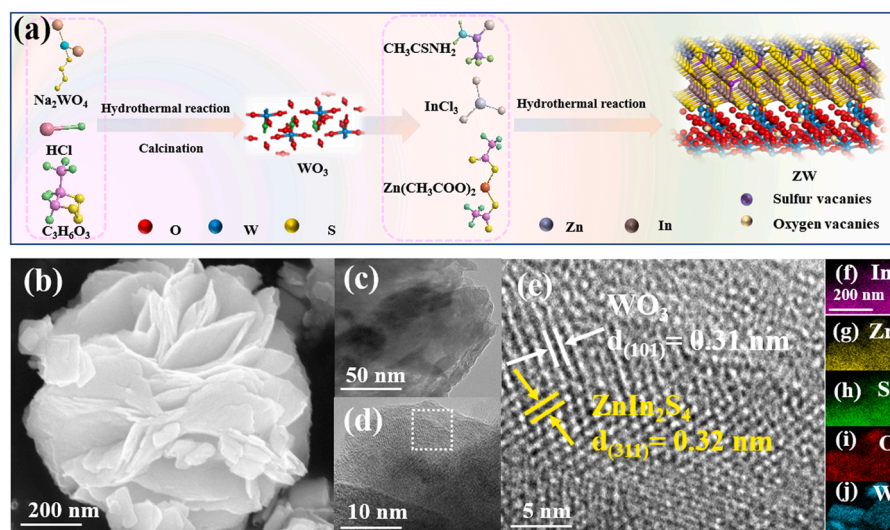


Fig. 1. (a) Schematic diagram of the synthesis process of ZW. (b) SEM images, (c) TEM images, (d-e) HRTEM images, and (f-j) the elemental mapping images of ZW-4.

WO_3 and RZW, suggesting that tight heterojunctions were formed [34]. On the other hand, DFT calculations have been performed to explore the interlayer distance. As shown in Fig. 2b-d, the interlayer distance of ZIS and WO_3 decreased from 4.83 to 2.44 nm after the introduction of vacancies, strongly confirming that interfacial bonds could be formed via introducing vacancies.

Moreover, the electronic structure of ZW-4 was investigated by XPS. The XPS full spectrum (Fig. S6, SI) indicated that ZW-4 samples contained O, Zn, W, In and S elements. Fig. 2e shows the peaks at 452.4 and 444.8 eV in the ZW-4, which corresponded to $\text{In } 3d_{5/2}$ and $\text{In } 3d_{3/2}$, respectively. In Fig. 2f, the two peaks of ZW-4 located at 1044.8 and 1021.8 eV are derived from $\text{Zn } 2p_{1/2}$ and $\text{Zn } 2p_{3/2}$, respectively [10]. Two peaks of ZW-4 (Fig. 2g) in high-resolution W 4f spectra located at 35.5 and 37.6 eV, corresponded to $\text{W } 4f_{7/2}$ and $\text{W } 4f_{5/2}$ levels of W-O bonding, and the peaks at higher binding energies can be attributed to W^{6+} species [32]. As displayed in the Fig. 2h, three peaks at 529.9, 531.4 and 532.4 eV are ascribed to the lattice O, oxygen vacancy and surface hydroxy [35,36]. On the other hand, the binding energies located at 162.9 eV ($\text{S } 2p_{1/2}$) and 161.6 eV ($\text{S } 2p_{3/2}$) (Fig. 2i) in ZW-4 are related to the S^{2-} state of ZnIn_2S_4 . Compared with RZW, the peaks of O 1s, Zn 2p and S 2p shifted towards lower binding energy in ZW-4. It may be due to the fact that the interface bonds formed by in situ growth between ZnIn_2S_4 and WO_3 changes its coordination environment, which leads to changing its electronic structure and valence environment, revealing that a strong chemical bond swingingly disturbed the electronic structure of WO_{3-x} and $\text{ZnIn}_2\text{S}_{4-x}$ [37]. More importantly, EPR characterization confirmed the type of atomic vacancy. In Fig. 2j, weak signals were detected in ZnIn_2S_4 and WO_3 at $g = 2.002$ and $g = 2.003$ [38], which account for O vacancies and S vacancies, respectively. It is noteworthy that ZW-4 shows a stronger and wider EPR signal around $g = 2.002$ – 2.003 , suggesting the existence of O vacancies and S vacancies at the same time. Moreover, the stronger the EPR signal is, the higher the unpaired electron is, and the more the vacancy concentration can be reflected [39,40]. Apart from this, ZW-4 possesses more spintronics, indicating that the interfacial bonds disturbed the electronic structure [41]. In general, the quadratic integral area is proportional to the vacancy concentration. According to the methods in the references [42, 43], the EPR data is further processed. We calculate the integral area of the ZW-4: RZW: WO_3 are 8.55, 4.96, 4.81 and 3.25, respectively. Therefore, the vacancy ratio of the ZW-4: RZW: ZIS: WO_3 is 2.63: 1.52: 1.48: 1, proving the interfacial bonds further disturbed the electronic structure. The existence of O and S vacancies in the ZW-4 catalyst were confirmed using high-angle annular dark-field scanning transmission

electron microscopy (HAADF-STEM). Fig. 2k exhibits a characteristic hexagonal pattern of ZnIn_2S_4 and WO_3 . Notably, sulfur vacancies and oxygen vacancies can be observed in the middle of the nanosheets (highlighted by dotted lines in the Fig. 2k and S7, SI), which is harmony with the simulation results (Fig. 2l) [44–46]. To confirm the category of vacancies, photoluminescence (PL) spectroscopy was carried out. As displayed in Fig. 3d, ZW exhibited two typical emission peaks at 567 and 486 nm. The emission can be ascribed to free exciton recombination through an exciton-exciton collision process, and the peak at 486 nm is caused by structural defects (such as oxygen vacancies) in the crystal, while the peak at 567 nm is caused by sulfur vacancies [47–49]. Above all, the EPR, HAADF-STEM and PL results confirmed the co-existence of S and O vacancies of ZW.

3.3. Investigation of charge-transfer behaviors

From the above electronic structure analysis, interfacial bonds tremendously affect electronic structure, which will disturb the electron transfer. Moreover, charge-transfer behaviors play an important role in photocatalytic performance. Therefore, we have implemented numerous investigations to clarify carrier migration behavior. Firstly, the energy band position determines the migration path of heterojunction. To reveal the optical properties of as-prepared samples, UV–vis diffuse reflectance spectroscopy (UV–vis DRS) was investigated. As shown in Fig. 3a, pure WO_3 and ZIS exhibited a steep absorption edge at approximately 450 and 570 nm. Interestingly, a gradual increase of light absorption can be observed, which originates from the enhanced amount of vacancies [50], suggesting that interfacial bonds disturbed the electronic structure. Accordingly, the bandgap of WO_3 and ZIS were 2.55 and 2.26 eV, respectively (Fig. S8, SI). From Fig. S9 (SI), the valence band (VB) of WO_3 and ZIS are 2.63 and 1.67 eV, respectively. Thus, the conduction band (CB) potential can be calculated as 0.08 and -0.59 eV for the WO_3 and ZIS, respectively (Fig. S10, SI) [51].

Considering band gaps positions of WO_3 and ZIS, two possible mechanisms of heterogeneous structures mechanisms (Z-scheme and type II) could be assumed (Fig. S11, SI). For the type II models, the photogenerated electrons and holes were located on the CB of WO_3 and VB of ZIS, respectively. Therefore, the positive reduction potential of ZW cannot satisfy the potential of $\text{E}(\text{H}^+/\text{H}_2, 0 \text{ V vs NHE})$. However, the following hydrogen production data conflicted with the type II models. It can be concluded that ZW is a typically direct Z-scheme heterogeneous. Thus, ZW has the thermodynamic potential for photocatalytic combined pollution degradation and hydrogen evolution [52].

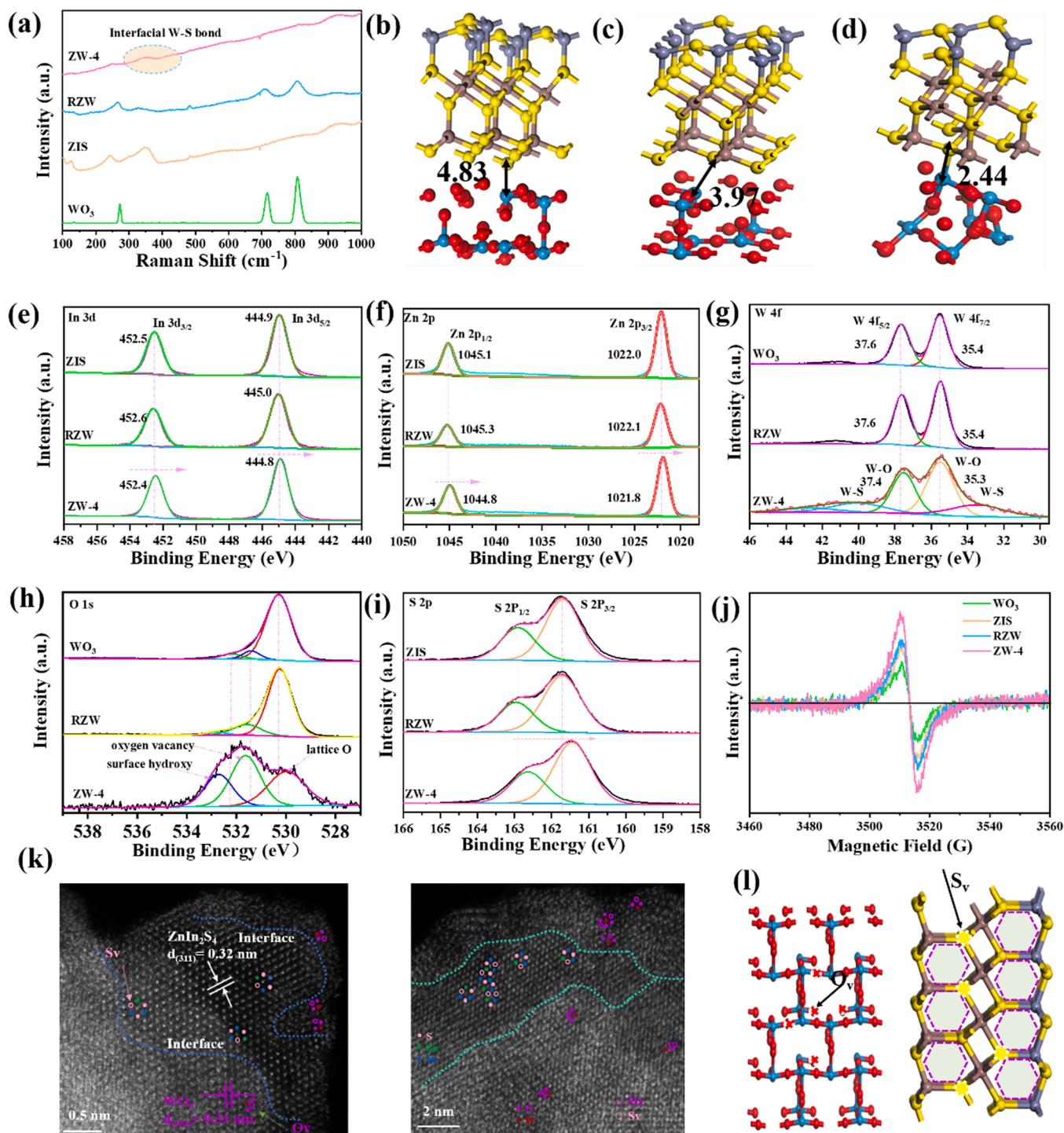


Fig. 2. (a) Raman spectra of as-prepared samples. (b) Interlayer distance of RZW without sulfur and oxygen vacancies. (c) Interlayer distance of RZW with sulfur and oxygen vacancies. (d) Interlayer distance of ZW with sulfur and oxygen vacancies. High-resolution XPS spectra of (e) In 3d, (f) Zn 2p, (g) W 4f, (h) O 1s and (i) S 2p. (j) EPR spectrum of WO₃, ZIS, RZW and ZW-4. (k) HAADF-STEM images and (l) simulation of ZW-4.

Based on the XPS results, the construction of a non-uniform interface between WO₃ and ZIS induced the distribution of internal electronic structure, which will affect charge distribution and form a built-in electric field (BE) [53]. It has been reported that the built-in electric field contains two factors: Zeta potential and surface potential. Therefore, the surface potential can be obtained by the atomic force microscopy with a Kelvin probe. Obviously, the surface potential of ZW-4 ($\Delta E = 41.2$ mV) is higher than that of RZW ($\Delta E = 8.9$ mV), WO₃ ($\Delta E = 7.3$ mV) and ZIS ($\Delta E = 24.6$ mV) (Fig. 3b). On the other hand, the Zeta

potentials of ZW-4, RZW, ZIS and WO₃ were found to be -67.3 , -30.7 , -53.8 and -21.0 mV, respectively (Table S1, SI). Therefore, the BE strength of ZW-4 sample is 3.63 times higher than that of WO₃ (Fig. 3c), which have been calibrated by open circuit potential. Strangely, the RZW exhibited lower BE strength than that of ZW, indicating that interfacial bonds contribute to interfacial electron transport in heterojunctions. Above all, enhanced BE provides a huge driving force to promote exciton dissociation and charge separation [54].

To characterize exciton dissociation in ZW, the photoluminescence

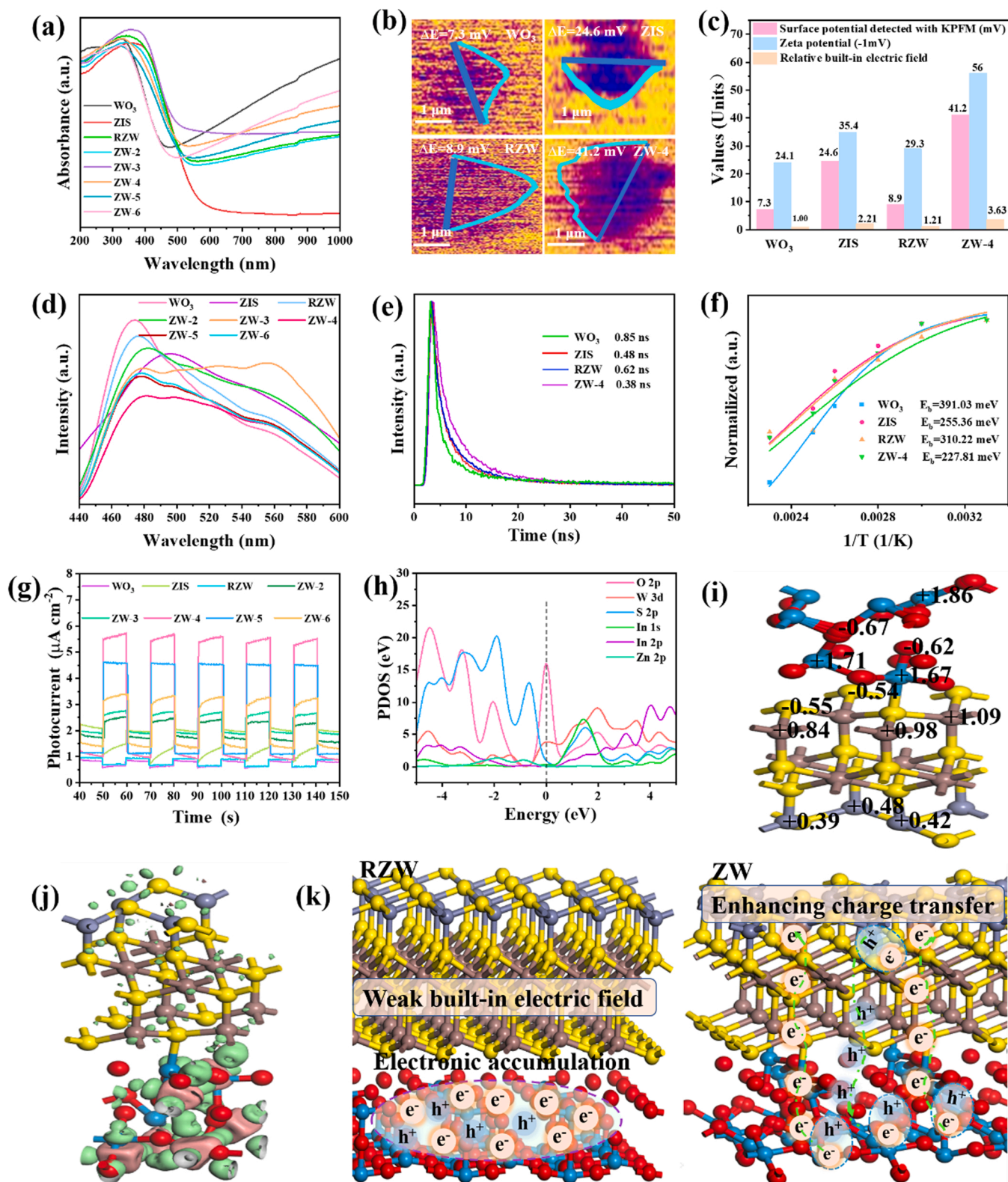


Fig. 3. (a) UV-vis diffuse reflectance spectra, (b) the surface potential, (c) the values of built-in electric field, (d) steady-state PL of samples, (e) time-resolved transient PL decay, (f) integrated PL intensity of samples as a function of temperature, and (g) photocurrent response spectra of the as prepared catalysts. (h) The projected density of states (PDOS), (i) charges on surface active sites, (j) electron density difference of ZW. (k) Schematic diagram of the electron transfer over as prepared samples.

(PL) spectra (Fig. 3d) has been explored. Compared to individual WO₃, ZIS and RZW, ZW-4 heterojunction shows reduced PL intensity, implying that a single exciton can break at the interfacial bonds of ZW to enhance the separation of electrons and holes [55,56]. As displayed in Fig. 3e, the average lifetime (τ) of charges for the ZW-4 hybrid is 0.38 ns, which is much shorter than that of RZW (0.62 ns), ZIS (0.48 ns) and WO₃ (0.85 ns) (Table S2, SI). The decreased fluorescence lifetime demonstrates the strong capability for the charge transfer and exciton dissociation [51]. The exciton binding energy (E_b) can be calculated from temperature-dependent photoluminescence spectra. From Fig. 3f and S12, the E_b of WO₃, ZIS, RZW and ZW-4 were calculated to be 391.03, 255.36, 310.22 and 227.81 meV, respectively. Compared with RZW, the introduced interfacial bonds disturbed the electronic structure, which provide a huge force to drive exciton dissociation.

To get more insight in the charge transfer, the photocurrent and electrochemical impedance spectroscopy (EIS) have been employed. As displayed in Fig. 3g, the photocurrent intensity follows the trend of ZW-4 > ZW-5 > ZW-6 > ZW-3 > ZW-2 > ZIS > RZW > WO₃, suggesting that interfacial bonds are beneficial to the charge transfer. Moreover, ZW-4 presents the smallest arc radius (Fig. S13, SI), suggesting the resistance of carrier migration in the heterojunction are greatly reduced.

To disclose the detailed electronic structure of the heterojunction, DFT calculations were carried out. Obviously, the VB of ZW is constructed by O orbits, and the CB is mainly dominated by W and In orbits (Fig. 3h and S14, SI). Compared with RZW, there are three bands (S s, W d and In p) across the Fermi level, which is derived from the entail metallicity of the nanoribbon [57]. For the RZW, metallicity occurred at WO₃, while there was a dramatic change in ZnIn₂S₄ for ZW, suggesting that interfacial bonds in ZW-4 severely enhanced strong electronic coupling, which contributes to charge transfer across the interface. Therefore, photogenerated electrons of WO₃ can transfer to ZIS under light irradiation with the assistance of built-in electric field, and hence possibly form a direct Z-scheme heterojunction [58]. In addition, the electrostatic potentials in surfaces of ZW (Fig. 3i) can further prove the electronic coupling of ZIS and WO₃ (Fig. S15, SI). For RZW, most of charge is concentrated on WO₃, and there is charge depletion on ZIS, suggesting that interfacial charge is impenetrable, resulting in a worse charge transfer rate and weaker BE. Once interfacial bonds are formed, charge depletion and aggregation shift to the surface of ZIS and WO₃, which is beneficial for the charge transfer of Z-scheme heterostructures. Moreover, the different electron density distribution and detailed charge analysis has been simulated (Fig. 3j and S16, SI). For RZW, the electrons located at the oxygen vacancy, suggesting counteractive charge transfer in the heterojunction, which is harmful for the formation of BE and carriers separation. Excitingly, the electrons can be delivered from WO₃ to the ZIS surface via the W-S bonds. On the other hand, the charge transfer routes can be explained from the work functions. As exhibited in Fig. S17 (SI), the work functions of WO₃, ZIS, RZW and ZW-4 are calculated to be 6.481, 4.968, 5.921 and 4.128 eV vs vacuum, suggesting that interior electrons tend to transfer from WO₃ to ZIS after their contact and form interfacial bonds. In addition, in situ Raman have been conducted to confirm the charge transfer in the interfacial bonds (Fig. S18, SI). The peak of ZW-4 at around 350 cm⁻¹ is W-S bond, while the peaks under light irradiation shifts towards lower wavelengths, suggesting the electron transfer bridge of W-S bonds.

Based on the above discussion, the detailed charge transfer routes were proposed (Fig. 3k). Under the Z-scheme mode, ZIS and WO₃ could generated electrons and holes. Once the interfacial bonds were formed, the electronic structure was disturbed and provide a huge force to drive the exciton dissociation and charge transfer. Therefore, electrons on the CB of WO₃ will recombine the VB holes of ZIS through the interface bonds. Meanwhile, photogenerated electrons in the CB of ZIS are transferred to the superficial S vacancies, and holes will transfer to the surface of WO₃ [59]. If interface bonds are missing, electrons exhibit interfacial convergence, which greatly hinders the formation of BE and results in deterioration of charge transfer and exciton dissociation.

Above all, the interfacial bonds tremendously regulate electronic structure for enhancing the compatibility of heterojunctions, which is estimated to exhibit excellent photocatalytic activity.

3.4. Photocatalytic activity and mechanism

Photocatalytic degradation of organic pollutants coupled with hydrogen generation (PPH) holds promise as a win-win strategy to produce clean energy and solve pollution problem. Therefore, we selected the photocatalytic degradation of RhB with the hydrogen production as the model reaction. As shown in Fig. 4a, WO₃ exhibits poor hydrogen production and RhB degradation, which is derived from the fact that the CB potential of WO₃ cannot satisfy the potential of hydrogen production. Besides, the hydrogen production rate of ZIS, RZW, ZW-2, ZW-3, ZW-4, ZW-5 and ZW-6 is 104.25, 35.50, 370.50, 400.00, 737.75, 490.50 and 437.75 $\mu\text{mol g}^{-1} \text{h}^{-1}$, respectively. The highest hydrogen production rate was achieved for the ZW-4 photocatalyst (Fig. 4b), which is almost 7 times as high as the value for the pristine ZIS. In addition, ZW-4 also exhibited the completely degradation activity (> 99.99%) (Fig. 4b). Importantly, under 405 nm monochromatic light illumination, the AQY of ZW-4 was calculated to be 0.76% (Fig. 4c), which is superior to others reported materials. Behind such outstanding performance, it can be decoded key factors of the interfacial bonds of ZW-4 enhancing the charge transfer. Moreover, surface properties could also affect photocatalytic performance. As shown in Fig. S19 (SI), the contact angle of organic pollutants is in the order: ZW-4 < ZW-5 < ZW-6 < ZW-3 < ZW-2 < ZIS < RZW < WO₃, implying that interfacial bonds disturbed electronic structure and relatively strengthened interaction with organic pollutants. To prove the origin of H⁺, D₂O isotope labeling measurements have been carried out. As exhibited in Fig. S20 (SI), an evident D₂ peak emerged, proving that the H₂ is not born in RhB but from water. In order to verify the degraded product, ¹H NMR has been performed on the reaction liquid after the reaction (Fig. S21, SI). Negligible organics were observed, suggesting ZW-4 have the highest degradation capacity. To test the stability of ZW-4, the five consecutive reactions have been implemented. As shown in Fig. 4d and S22 (SI), the degradation of RhB and H₂ generation of ZW-4 remained highly stability after five cycles. From XRD (Fig. S23, SI) and XPS patterns (Fig. S24, SI), no evident destruction can be observed, suggesting the ZW-4 has excellent application prospects.

To verify the universality of ZW-4, simultaneous hydrogen production and degradation and of other substances were also performed. As shown in Fig. 4e, ZW-4 also achieve a remarkable hydrogen production rate and degradation rate. Moreover, the wastewater from the production of liquor was considered as a reactant. The detailed component can be seen in our reported works. Notably, the COD value over ZW-4 is 293 mg L⁻¹, while the COD of the origin wastewater is 408 mg L⁻¹ (Fig. S25, SI). Therefore, the prepared samples could act as potential candidates for the simultaneous degradation of organic pollutant and hydrogen production.

As we all know, the H⁺ can be reacted with e⁻ to form H₂. However, the active species of photocatalytic degradation of organic pollutant is still controversial. Therefore, quenching experiments in RhB solution have been implemented. As shown in Fig. S26 (SI), the h⁺ and •OH play a dominant role in the photocatalytic degradation of RhB. Moreover, we use the in situ FT-IR to observe the degradation processes. As exhibited in Fig. S27 (SI), a slight peak around 2350 cm⁻¹ is assigned to CO₂, implying the RhB has been degraded by ZW-4 [60]. The broad peak around 3710 cm⁻¹ is related to the adsorbed H₂O [61]. In our system, the Gibbs free energy calculations provide insight into the nature of the reaction process. As shown in Fig. 4f, ZW-4 manifested the lowest energy barrier in H₂ generation, which has been confirmed by the experimental data, indicating that ZW-4 is more favorable for H₂ production. In addition, DFT calculations confirmed that the introduction of S defects favors H₂ evolution.

According to the aforementioned results, the mechanism of PPH over

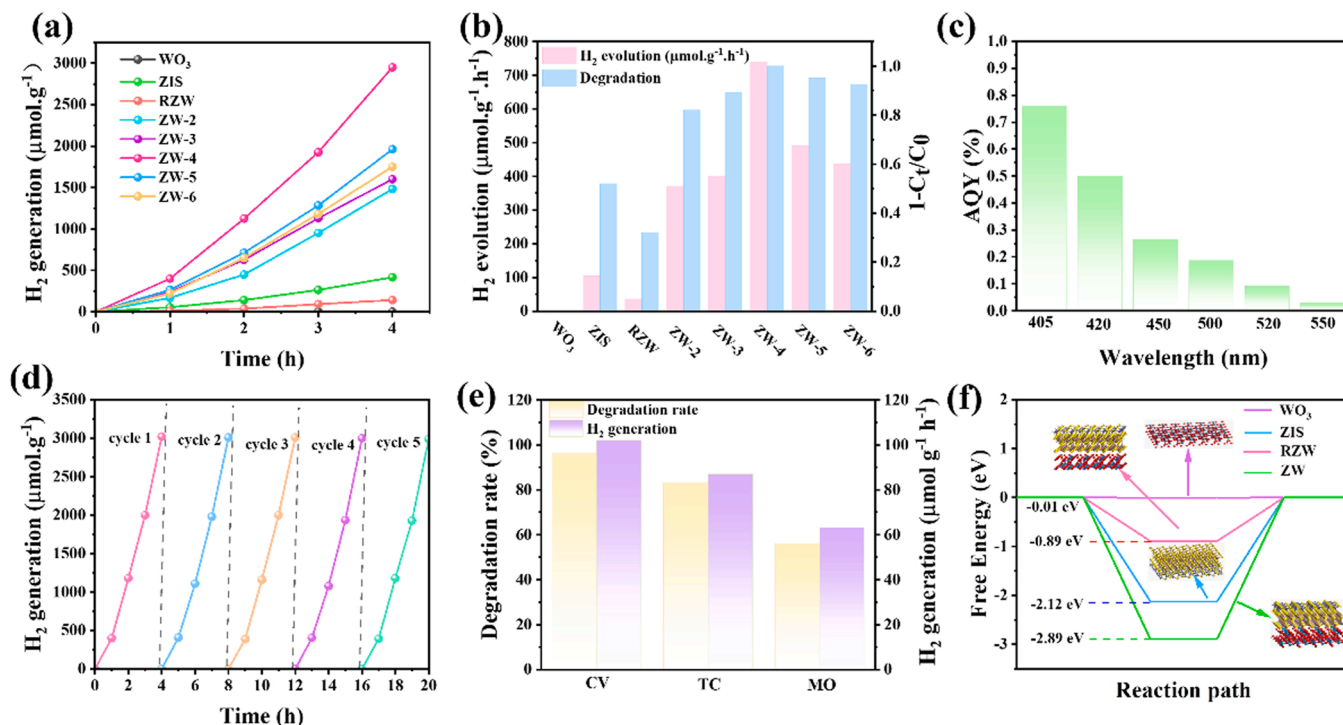


Fig. 4. (a) H₂ generation of as-prepared samples. (b) H₂ generation and RhB degradation for 4 h. (c) AQY of H₂ generation over ZW-4. (d) Stability of ZW-4 during the photocatalytic H₂ generation. (e) The degradation rate and H₂ generation of crystal violet (CV), tetracycline (TC) and methyl orange (MO). (f) DFT-calculated Gibbs free energy of H₂ generation.

ZW-4 can be proposed (Fig. 5). Under visible light irradiation, both ZIS and WO₃ could generate electrons and holes. Due to the Z-scheme heterojunction of ZIS and WO₃, electrons on the CB of WO₃ will recombine the VB holes of ZIS through the interface bonds. Meanwhile, photo-generated electrons in the CB of ZIS are transferred to the superficial S vacancies, and holes will transfer to the surface of WO₃. Moreover, the sulfur vacancies also provide active sites to H⁺ reduction for improving hydrogen production performance. The h⁺ will oxidize water to form •OH, which subsequently applied to the RhB. In this work, h⁺ and •OH are the main active species for RhB degradation [62], while H₂ is produced by the contribution of electrons to reduce water.

4. Conclusions

In summary, the ultrathin ZnIn₂S_{4-x}-WO_{3-x} Z-scheme heterostructure (ZW) was synthesized via a facile in situ hydrothermal strategy. Moreover, dual vacancies induced the formation of interfacial bonds. Experimental results and DFT calculations testified that the interfacial bonds tremendously regulated strong electronic coupling of ZnIn₂S_{4-x}-WO_{3-x} to enhance the compatibility of the heterojunction. Firstly, the strong electronic coupling of ZnIn₂S_{4-x}-WO_{3-x} enlarged the built-in electric field and reduced the aggregation effect of charge in interfacial vacancies, which is contributed to promoting charge transfer through the interface and exciton dissociation. On the other hand, it not only improved surface reactivity, but also provided the active sites for reducing the catalytic energy barrier. Ultimately, the optimized ZW-4 exhibited an exceptional photocatalytic hydrogen evolution performance of 737.75 μmol g⁻¹ h⁻¹ and a pollution degradation rate greater than 99.99% without using any cocatalyst under visible light irradiation (Table S3, SI). We hope that this study will provide new perspectives for the design and application of direct Z-scheme heterojunction with great potential in solving environmental pollution and energy crises.

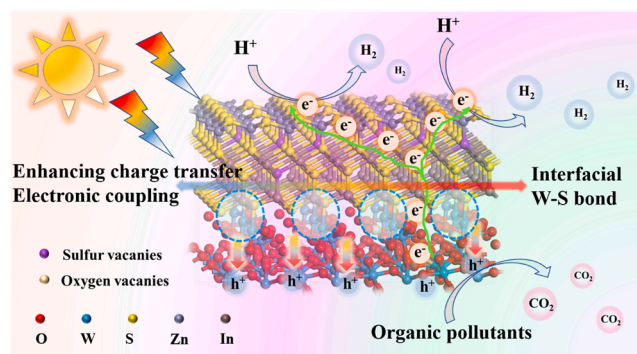


Fig. 5. Plausible mechanism for the PPH over ZW.

CRediT authorship contribution statement

Xiaomei Sun: Methodology, Experiment, Data curation, Writing-review & editing **Meiyang Song:** Investigation, Experiment. **Fei Liu:** Supervision, Investigation. **Haiyan Peng:** Investigation. **Tianxiang Zhao:** Supervision, Investigation. **Shuang-Feng Yin:** Supervision, Investigation. **Peng Chen:** Conceptualization, Monitoring, Rewriting-review & editing, Formal analysis, Funding acquisition.

Declaration of Competing Interest

The authors declare that they have no known competing financial interests or personal relationships that could have appeared to influence the work reported in this paper.

Data availability

Data will be made available on request.

Acknowledgments

This project was financially supported by Science and Technology Support Program of Guizhou Province (General Project) (No. 2023089), Guizhou Provincial Basic Research Program (Natural Science) (No. ZK2021069 and ZK2023049), Young Science and Technology Talents Development Project of Education Department in Guizhou Province (No. KY2022144), National Natural Science Foundation of China (No. 22268015), Innovation Group Project of Education Department in Guizhou Province (No. 2021010), Key Laboratory of Carbon-based Energy Molecular Chemical Utilization Technology in Guizhou Province (No.2023008). The authors would like to thank Shiyanjia Lab (www.shiyanjia.com) for materials characterizations, and thanks for the computing support of the State Key Laboratory of Public Big Data, Guizhou University.

Appendix A. Supporting information

Supplementary data associated with this article can be found in the online version at [doi:10.1016/j.apcatb.2023.123436](https://doi.org/10.1016/j.apcatb.2023.123436).

References

- [1] S. Wang, Y. Wang, S.L. Zhang, S.Q. Zang, X.W. Lou, Supporting ultrathin ZnIn_2S_4 nanosheets on Co/N-doped graphitic carbon nanocages for efficient photocatalytic H_2 generation, *Adv. Mater.* 31 (41) (2019), e1903404.
- [2] S. Wang, B.Y. Guan, X.W. Lou, Construction of ZnIn_2S_4 - In_2O_3 hierarchical tubular heterostructures for efficient CO_2 photoreduction, *J. Am. Chem. Soc.* 140 (15) (2018) 5037–5040.
- [3] T. Su, Q. Shao, Z. Qin, Z. Guo, Z. Wu, Role of interfaces in two-dimensional photocatalyst for water splitting, *ACS Catal.* 8 (3) (2018) 2253–2276.
- [4] D. Gao, J. Xu, L. Wang, B. Zhu, H. Yu, J. Yu, Optimizing atomic hydrogen desorption of sulfur-rich NiS_{1+x} cocatalyst for boosting photocatalytic H_2 evolution, *Adv. Mater.* 34 (6) (2022), e2108475.
- [5] H. Li, B. Chong, B. Xu, N. Wells, X. Yan, G. Yang, Nanoconfinement-induced conversion of water chemical adsorption properties in nanoporous photocatalysts to improve photocatalytic hydrogen evolution, *ACS Catal.* 11 (22) (2021) 14076–14086.
- [6] C. Bie, B. Zhu, L. Wang, H. Yu, C. Jiang, T. Chen, J. Yu, A bifunctional $\text{CdS}/\text{MoO}_3/\text{MoS}_2$ catalyst enhances photocatalytic H_2 evolution and pyruvic acid synthesis, *Angew. Chem. Int. Ed.* 61 (44) (2022), 202212045.
- [7] P.V. Kumar, M.P. Short, S. Yip, B. Yildiz, J.C. Grossman, High surface reactivity and water adsorption on NiFe_2O_4 (111) surfaces, *J. Phys. Chem. C* 117 (11) (2013) 5678–5683.
- [8] Z. Li, W. Huang, J. Liu, K. Lv, Q. Li, Embedding CdS/Au into ultrathin $\text{Ti}_3\text{-xC}_2\text{Ty}$ to build dual schottky barriers for photocatalytic H_2 production, *ACS Catal.* 11 (14) (2021) 8510–8520.
- [9] Z. Lin, J. Li, W. Shen, J.-P. Corriou, X. Chen, H. Xi, Different photocatalytic levels of organics in papermaking wastewater by flocculation-photocatalysis and SBR-photocatalysis: degradation and GC-MS experiments, adsorption and photocatalysis simulations, *Chem. Eng. J.* 412 (2021), 128715.
- [10] S. Liu, X. Zhou, J. Qin, C. Wei, Y. Hu, 3-D nitrogen-doped carbon cage encapsulated ultrasmall MoC nanoparticles for promoting simultaneous ZnIn_2S_4 photocatalytic hydrogen generation and organic wastewater degradation, *J. Colloid Interfaces Sci.* 635 (2023) 59–71.
- [11] C. Liu, Q. Zhang, Z. Zou, Recent advances in designing ZnIn_2S_4 -based heterostructured photocatalysts for hydrogen evolution, *J. Mater. Sci. Technol.* 139 (2023) 167–188.
- [12] K. Wang, Z. Huang, J. Wang, Synthesis of hierarchical tandem double Z-scheme heterojunctions for robust photocatalytic H_2 generation, *Chem. Eng. J.* 430 (2022), 132727.
- [13] W. Jiang, X. Zong, L. An, S. Hua, X. Miao, S. Luan, Y. Wen, F.F. Tao, Z. Sun, Consciously constructing heterojunction or direct Z-scheme photocatalysts by regulating electron flow direction, *ACS Catal.* 8 (3) (2018) 2209–2217.
- [14] N.A. Mohd Razali, W.N. Wan Salleh, F. Aziz, L.W. Jye, N. Yusof, A.F. Ismail, Review on tungsten trioxide as a photocatalysts for degradation of recalcitrant pollutants, *J. Clean. Prod.* 309 (2021), 127438.
- [15] X. Zheng, Y. Song, Y. Liu, Y. Yang, D. Wu, Y. Yang, S. Feng, J. Li, W. Liu, Y. Shen, X. Tian, ZnIn_2S_4 -based photocatalysts for photocatalytic hydrogen evolution via water splitting, *Coord. Chem. Rev.* 475 (2023), 214898.
- [16] M. Tang, Y. Ao, P. Wang, C. Wang, All-solid-state Z-scheme WO_3 nanorod/ ZnIn_2S_4 composite photocatalysts for the effective degradation of nitenpyram under visible light irradiation, *J. Hazard. Mater.* 387 (2020), 121713.
- [17] Z. Li, J. Hou, B. Zhang, S. Cao, Y. Wu, Z. Gao, X. Nie, L. Sun, Two-dimensional Janus heterostructures for superior Z-scheme photocatalytic water splitting, *Nano Energy* 59 (2019) 537–544.
- [18] H.S. Moon, K.C. Hsiao, M.C. Wu, Y. Yun, Y.J. Hsu, K. Yong, Spatial separation of cocatalysts on Z-scheme organic/inorganic heterostructure hollow spheres for enhanced photocatalytic H_2 evolution and in-depth analysis of the charge-transfer mechanism, *Adv. Mater.* 35 (4) (2023), e2200172.
- [19] X. Ruan, C. Huang, H. Cheng, Z. Zhang, Y. Cui, Z. Li, T. Xie, K. Ba, H. Zhang, L. Zhang, X. Zhao, J. Leng, S. Jin, W. Zhang, W. Zheng, S.K. Ravi, Z. Jiang, X. Cui, J. Yu, A twin S-scheme artificial photosynthetic system with self-assembled heterojunctions yields superior photocatalytic hydrogen evolution rate, *Adv. Mater.* 35 (6) (2023), e2209141.
- [20] W.-P. Hsu, M. Mishra, W.-S. Liu, C.-Y. Su, T.-P. Perng, Fabrication of direct Z-scheme Ta_3N_5 - $\text{WO}_{2.72}$ film heterojunction photocatalyst for enhanced hydrogen evolution, *Appl. Catal. B: Environ.* 201 (2017) 511–517.
- [21] G. Li, X. Deng, P. Chen, X. Wang, J. Ma, F. Liu, S.-F. Yin, Sulphur vacancies- VS_2 @ C_3N_4 driven by in situ supramolecular self-assembly for synergistic photocatalytic degradation of real wastewater and H_2 production: vacancies taming interfacial compact heterojunction and carriers transfer, *Chem. Eng. J.* 433 (2022), 134505.
- [22] H. Peng, X. Deng, G. Li, Q. Wang, M. Song, P. Chen, S.-F. Yin, Oxygen vacancy and van der Waals heterojunction modulated interfacial chemical bond over $\text{Mo}_2\text{C}/\text{Bi}_4\text{O}_5\text{Br}_2$ for boosting photocatalytic CO_2 reduction, *Appl. Catal. B: Environ.* 318 (2022), 121866.
- [23] X. Lian, Z. Huang, Y. Zhang, Z. Chen, P. Meidl, X. Yi, B. Xu, Constructing Z-scheme 1D/2D heterojunction of ZnIn_2S_4 nanosheets decorated WO_3 nanorods to enhance Cr(VI) photocatalytic reduction and rhodamine B degradation, *Chemosphere* 313 (2023), 137351.
- [24] Z. Hu, X. Liu, P.L. Hernández-Martínez, S. Zhang, P. Gu, W. Du, W. Xu, H.V. Demir, H. Liu, Q. Xiong, Interfacial charge and energy transfer in van der Waals heterojunctions, *InfoMat* 4 (3) (2022) 12290.
- [25] M. Zhang, J. Yao, M. Arif, B. Qiu, H. Yin, X. Liu, S.-m. Chen, 0D/2D $\text{CeO}_2/\text{ZnIn}_2\text{S}_4$ Z-scheme heterojunction for visible-light-driven photocatalytic H_2 evolution, *Appl. Surf. Sci.* 526 (2020), 145749.
- [26] L. Li, D. Ma, Q. Xu, S. Huang, Constructing hierarchical $\text{ZnIn}_2\text{S}_4/\text{g-C}_3\text{N}_4$ S-scheme heterojunction for boosted CO_2 photoreduction performance, *Chem. Eng. J.* 437 (2022), 135153.
- [27] Z. Wei, W. Wang, W. Li, X. Bai, J. Zhao, E.C.M. Tse, D.L. Phillips, Y. Zhu, Steering electron-hole migration pathways using oxygen vacancies in tungsten oxides to enhance their photocatalytic oxygen evolution performance, *Angew. Chem. Int. Ed.* 60 (15) (2021) 8236–8242.
- [28] Z. Wang, C. Zhu, Z. Ni, H. Hojo, H. Einaga, Enhanced photocatalytic benzene oxidation to phenol over monoclinic WO_3 nanorods under visible light, *ACS Catal.* 12 (24) (2022) 14976–14989.
- [29] C. Du, Q. Zhang, Z. Lin, B. Yan, C. Xia, G. Yang, Half-unit-cell ZnIn_2S_4 monolayer with sulfur vacancies for photocatalytic hydrogen evolution, *Appl. Catal. B: Environ.* 248 (2019) 193–201.
- [30] Y. Ding, D. Wei, R. He, R. Yuan, T. Xie, Z. Li, Rational design of Z-scheme $\text{PtS}/\text{ZnIn}_2\text{S}_4/\text{WO}_3$ - MnO_2 for overall photo-catalytic water splitting under visible light, *Appl. Catal. B: Environ.* 258 (2019), 117948.
- [31] L. Zhang, J. Qiu, D. Dai, Y. Zhou, X. Liu, J. Yao, Cr-metal-organic framework coordination with ZnIn_2S_4 nanosheets for photocatalytic reduction of Cr(VI), *J. Clean. Prod.* 341 (2022), 130891.
- [32] T. Van Nguyen, H.H. Do, M. Tekalgne, Q. Van Le, T.P. Nguyen, S.H. Hong, J. H. Cho, D. Van Dao, S.H. Ahn, S.Y. Kim, WS_2 - WC/WO_3 nano-hollow spheres as an efficient and durable catalyst for hydrogen evolution reaction, *Nano Converg.* 8 (1) (2021), 28.
- [33] D.-B. Seo, S. Yoo, V. Dongquoc, T.N. Trung, E.-T. Kim, Facile synthesis and efficient photoelectrochemical reaction of WO_3/WS_2 core@shell nanorods utilizing $\text{WO}_3\cdot 0.33\text{H}_2\text{O}$ phase, *J. Alloy. Compd.* 888 (2021), 161587.
- [34] S. Zhan, H. Zhang, Y. Zhang, Q. Shi, Y. Li, X. Li, Efficient NH_3 -SCR removal of NO_x with highly ordered mesoporous $\text{WO}_3(\text{x})$ - CeO_2 at low temperatures, *Appl. Catal. B: Environ.* 203 (2017) 199–209.
- [35] B. Wang, Z. Cai, J. Zhong, J. Li, Rich oxygen vacancies facilitated photocatalytic performance of BiOBr induced by carbon black, *Solid State Sci.* 132 (2022), 106985.
- [36] N. Zhang, L. Li, Q. Shao, T. Zhu, X. Huang, X. Xiao, Fe-doped BiOCl nanosheets with light-switchable oxygen vacancies for photocatalytic nitrogen fixation, *ACS Appl. Mater. Sci.* 2 (2019) 8394–8398.
- [37] J.Y. Li, C.L. Tan, M.Y. Qi, Z.R. Tang, Y.J. Xu, Exposed zinc sites on hybrid ZnIn_2S_4 @ CdS nanocages for efficient regioselective photocatalytic epoxide alcoholysis, *Angew. Chem. Int. Ed.* 62 (2023), e202303054.
- [38] G. Zhang, J. Yang, Z. Huang, G. Pan, B. Xie, Z. Ni, S. Xia, Construction dual vacancies to regulate the energy band structure of ZnIn_2S_4 for enhanced visible light-driven photodegradation of 4-NP, *J. Hazard. Mater.* 441 (2023), 129916.
- [39] A. Kumar, P. Singh, V.-H. Nguyen, Q. Van Le, T. Ahamad, S. Thakur, L. Huong Nguyen, P. Raizada, Rationally constructed synergy between dual-vacancies and Z-scheme heterostructured MoS_2 - $\text{x/g-C}_3\text{N}_4/\text{Ca-}\alpha\text{-Fe}_2\text{O}_3$ for high-performance photodegradation of sulfamethoxazole antibiotic from aqueous solution, *Chem. Eng. J.* 474 (2023), 145720.
- [40] J. Jiang, X. Wang, Q. Xu, Z. Mei, L. Duan, H. Guo, Understanding dual-vacancy heterojunction for boosting photocatalytic CO_2 reduction with highly selective conversion to CH_4 , *Appl. Catal. B: Environ.* 316 (2022), 121679.
- [41] Q. Wang, H. Xu, X. Qian, G. He, H. Chen, Oxygen and sulfur dual vacancy engineering on a 3D $\text{Co}_3\text{O}_4/\text{CoS}_4$ heterostructure to improve overall water splitting activity, *Green. Chem.* 24 (23) (2022) 9220–9232.
- [42] Y. Zhang, M. Zhang, Y. Liu, H. Zhu, L. Wang, Y. Liu, M. Xue, B. Li, X. Tao, Oxygen vacancy regulated TiNb_2O_7 compound with enhanced electrochemical performance used as anode material in Li-ion batteries, *Electrochim. Acta* 330 (2020), 135299.

- [43] F. Wang, L. Mao, X. Qi, L. Xia, H. Xie, J. Mao, Sulfur-induced abundant oxygen vacancies in hollow silica microsphere toward super anode, *Chem. Eng. J.* 418 (2021), 129397.
- [44] G. Liu, A.W. Robertson, M.M.-J. Li, W.C.H. Kuo, M.T. Darby, M.H. Muhieddine, Y.-C. Lin, K. Suenaga, M. Stamatakis, J.H. Warner, S.C.E. Tsang, MoS₂ monolayer catalyst doped with isolated Co atoms for the hydrodeoxygenation reaction, *Nat. Chem.* 9 (2017) 810–816.
- [45] J. Hu, L. Yu, J. Deng, Y. Wang, K. Cheng, C. Ma, Q. Zhang, W. Wen, S. Yu, Y. Pan, J. Yang, H. Ma, F. Qi, Y. Wang, Y. Zheng, M. Chen, R. Huang, S. Zhang, Z. Zhao, J. Mao, X. Meng, Q. Ji, G. Hou, X. Han, X. Bao, Y. Wang, D. Deng, Sulfur vacancy-rich MoS₂ as a catalyst for the hydrogenation of CO₂ to methanol, *Nat. Catal.* 4 (2021) 242–250.
- [46] C. Peng, G. Luo, J. Zhang, M. Chen, Z. Wang, T.-K. Sham, L. Zhang, Y. Li, G. Zheng, Double sulfur vacancies by lithium tuning enhance CO₂ electroreduction to n-propanol, *Nat. Commun.* 12 (2021) 1580.
- [47] R. Liang, C. Shu, A. Hu, C. Xu, R. Zheng, M. Li, Y. Guo, M. He, Y. Yan, J. Long, Tuning the electronic band structure of Mott-Schottky heterojunctions modified with surface sulfur vacancy achieves an oxygen electrode with high catalytic activity for lithium-oxygen batteries, *J. Mater. Chem. A* 8 (22) (2020) 11337–11345.
- [48] H. Zhu, X. Song, X. Han, X. Zhang, J. Bao, N. Zhang, G. He, Co₃O₄ Nanosheets preferentially growing (220) facet with a large amount of surface chemisorbed oxygen for efficient oxidation of elemental mercury from flue gas, *Environ. Sci. Technol.* 54 (14) (2020) 8601–8611.
- [49] Q. Wang, H. Xu, X. Qian, G. He, H. Chen, Oxygen and sulfur dual vacancy engineering on a 3D Co₃O₄/Co₃S₄ heterostructure to improve overall water splitting activity, *Green Chem.* 24 (23) (2022) 9220–9232.
- [50] T. Su, C. Men, L. Chen, B. Chu, X. Luo, H. Ji, J. Chen, Z. Qin, Sulfur vacancy and Ti₃C₂T_x cocatalyst synergistically boosting interfacial charge transfer in 2D/2D Ti₃C₂T_x/ZnIn₂S₄ heterostructure for enhanced photocatalytic hydrogen evolution, *Adv. Sci.* 9 (4) (2022), 2103715.
- [51] M. Zhao, S. Liu, D. Chen, S. Zhang, S.A.C. Carabineiro, K. Lv, A novel S-scheme 3D ZnIn₂S₄/WO₃ heterostructure for improved hydrogen production under visible light irradiation, *Chin. J. Catal.* 43 (10) (2022) 2615–2624.
- [52] H. Sepehrmansourie, H. Alamgholiloo, N. Noroozi Pesyan, M.A. Zolfigol, A MOF-on-MOF strategy to construct double Z-scheme heterojunction for high-performance photocatalytic degradation, *Appl. Catal. B: Environ.* 321 (2023), 122082.
- [53] X. Wang, X. Wang, J. Huang, S. Li, A. Meng, Z. Li, Interfacial chemical bond and internal electric field modulated Z-scheme S_v-ZnIn₂S₄/MoSe₂ photocatalyst for efficient hydrogen evolution, *Nat. Commun.* 12 (1) (2021), 4112.
- [54] Y. Sheng, W. Li, L. Xu, Y. Zhu, High photocatalytic oxygen evolution via strong built-in electric field induced by high crystallinity of perylene imide supramolecule, *Adv. Mater.* 34 (10) (2022), e2102354.
- [55] V. Ramar, K. Balasubramanian, Charge transfer induced tunable bandgap and enhanced saturable absorption behavior in rGO/WO₃ composites, *Appl. Phys. A* 124 (11) (2018), 779.
- [56] M. Tan, Y. Ma, C. Yu, Q. Luan, J. Li, C. Liu, W. Dong, Y. Su, L. Qiao, L. Gao, Q. Lu, Y. Bai, Boosting photocatalytic hydrogen production via interfacial engineering on 2D ultrathin Z-scheme ZnIn₂S₄/g-C₃N₄ heterojunction, *Adv. Funct. Mater.* 32 (14) (2021), 2111740.
- [57] Q. Luan, X. Xue, R. Li, L. Gu, W. Dong, D. Zhou, X. Wang, B. Li, G. Wang, C. Hou, Boosting photocatalytic hydrogen evolution: orbital redistribution of ultrathin ZnIn₂S₄ nanosheets via atomic defects, *Appl. Catal. B: Environ.* 305 (2022), 121007.
- [58] F. Xing, C. Wang, S. Liu, S. Jin, H. Jin, J. Li, Interfacial chemical bond engineering in a direct Z-scheme g-C₃N₄/MoS₂ heterojunction, *ACS Appl. Mater. Interfaces* 15 (9) (2023) 11731–11740.
- [59] M. Chen, D. Liu, L. Qiao, P. Zhou, J. Feng, K.W. Ng, Q. Liu, S. Wang, H. Pan, *In-situ/operando* Raman techniques for in-depth understanding on electrocatalysis, *Chem. Eng. J.* 461 (2023), 141939.
- [60] Y. Zhang, J. Di, X. Zhu, M. Ji, C. Chen, Y. Liu, L. Li, T. Wei, H. Li, J. Xia, Chemical bonding interface in Bi₂Sn₂O₇/BiOBr S-scheme heterojunction triggering efficient N₂ photofixation, *Appl. Catal. B: Environ.* 323 (2023), 122148.
- [61] H. Khosropour, B. Rezaei, P. Rezaei, A.A. Ensafi, Ultrasensitive voltammetric and impedimetric aptasensor for diazinon pesticide detection by VS₂ quantum dots-graphene nanoplatelets/carboxylated multiwalled carbon nanotubes as a new group nanocomposite for signal enrichment, *Anal. Chim. Acta* 1111 (2020) 92–102.
- [62] M.A. Barakat, R. Kumar, T. Almeelbi, B.A. Al-Mur, J.O. Eniola, Sustainable visible light photocatalytic scavenging of the noxious organic pollutant using recyclable and reusable polyaniline coupled WO₃/WS₂ nanohybrid, *J. Clean. Prod.* 330 (2022), 129942.